
Plasmapheresis in Radioimmunotherapy of Micrometastases: A Mathematical Modeling and Dosimetrical Analysis

George Sgouros

Department of Medical Physics, Memorial Sloan-Kettering Cancer Center, New York, New York

The feasibility of combining plasmapheresis with a large administration of radiolabeled antibody in order to overcome the "binding-site" barrier to antibody penetration in targeting hematologically distributed micrometastases is examined. In such a strategy, intravenous administration of excess radiolabeled antibody, to saturate antigen sites on the cell cluster periphery, is followed by removal of unbound antibody from the plasma, by plasmapheresis, to reduce the absorbed dose to the red marrow. Plasma antibody kinetics are simulated by a non-linear compartmental model representing free and antigen-bound antibody. This provides the boundary condition for a model of antibody diffusion, saturable binding to and dissociation from antigen sites within a 200 μm diameter cluster of tumor cells. Using these models, the absorbed dose to the red marrow and the absorbed dose profile across the cell cluster are calculated. Changes in marrow and cell cluster absorbed dose from alterations in the onset time and rate of plasmapheresis are illustrated for antibody labeled with ^{123}I , ^{125}I and ^{131}I . The results demonstrate that the "binding site" barrier may be overcome, yielding a 2- to 100-fold improvement in the cell cluster absorbed dose for a given bone marrow absorbed dose.

J Nucl Med 1992; 33:2167-2179

The successful implementation of radioimmunotherapy for treatment of cancer has proven to be considerably more difficult than initially anticipated (1-4). This is, in large part, because of the highly diverse, complex and interrelated biological and physical factors that must be considered in devising a successful protocol. In broad terms, the biological factors include the route and amount of administered monoclonal antibody (5-9), whether it is intact antibody or an antibody fragment (10-12), whether it is mouse-, human-derived or chimeric (13,14) and whether post- or pre-administration interventions are employed. Such interventions include the administration of unlabeled antibody (15,17), agents that alter tumor-cell

antigen-expression (18-21), agents that enhance tumor tissue permeability (20,22), and plasmapheresis (23-29).

Using mathematical models that incorporate plasma antibody pharmacokinetics, extravasation and interstitial transport and the antibody-antigen interaction, Fujimori, et al. and van Osdol et al. (30-33) have examined the relationship between a variety of tumor- and antibody-specific parameters and the microscopic distribution of antibody and absorbed dose within a tumor. A principal finding of this work has been the characterization of a "binding-site" barrier. The antibody is, in effect, prevented from diffusing to the interior of the tumor until the antigen sites in the periphery are occupied. Under expected in vivo conditions, the binding-site barrier results in a highly nonuniform antibody distribution within the tumor. In large, vascularized, solid tumors, this problem is compounded by poor lymphatic drainage that results in elevated interstitial fluid pressure (34). The effect of this on antibody distribution has been studied extensively by Jain and co-workers (35,36). As part of a more general pharmacokinetic analysis of two-step antibody approaches, Yuan et al. (37) have examined the effect of bifunctional and enzyme-conjugated antibody removal from the plasma prior to injection of the hapten or prodrug, respectively. Using extensive biodistribution data obtained from a rat model, Norrgren and co-workers, have developed a multi-compartmental model of antibody distribution and have used this to simulate plasmapheresis and to evaluate the resulting diagnostic and therapeutic gains (25,27). Hartmann et al. have fit a two-compartment model to plasma data from patients that underwent extracorporeal immunoadsorption following radiolabeled antibody administration (26).

This work examines the feasibility of combining plasmapheresis with a large administration of radiolabeled antibody in order to overcome the binding-site barrier in targeting hematologically distributed micrometastases. Subsequent removal of unbound antibody from the plasma by plasmapheresis serves to reduce the absorbed dose to the red marrow. The simulations focus on micrometastatic clusters of cells that are on the luminal side of the basement membrane. This geometry is different from previously described models in that the intravenously ad-

Received Feb. 4, 1992; revision accepted June 11, 1992.
For reprints contact: George Sgouros, PhD, Department of Medical Physics, Memorial Sloan-Kettering Cancer Center, 1275 York Ave., New York, NY 10021.

ministered antibody is directly accessible to the tumor cell cluster (i.e., the basement membrane and the interstitial fluid pressure are eliminated as barriers to achieving a uniform distribution of antibody within the cell cluster). Such a scenario is consistent with the early stage of micrometastatic spread (38) and presents the opportunity for antibody targeting of disseminated disease prior to antibody extravasation.

METHODS

Macroscopic Model

Micrometastases on the Luminal Side of the Basement Membrane. A tumor burden of 10 g [approximately 10^{10} cells (39)] is assumed to be distributed throughout a 3.8 l volume (V_d), corresponding to the plasma (31) and the sum of the liver, spleen and red bone marrow extracellular fluid volumes [0.48, 0.05 and 0.221, respectively (40)]. Due to the near absence of a developed capillary basement membrane in the latter three tissues (41,42), tumor cells lodged within these tissues are assumed directly accessible to intravenously administered radiolabeled antibody.

Depending upon the total amount administered, the antibody is infused over a period of 1 or 2 hr.

Antibody infusion, plasmapheresis and clearance from plasma and from the liver, spleen and red bone marrow extracellular spaces as well as saturable binding of antibody to and dissociation from antigen sites on tumor cells was simulated on a VAX 8810 computer (Digital Equipment Corporation, Maynard, MA) using version 30 of the simulation analysis and modeling (SAAM) program developed by Berman et al. (43) and supported by the Resource Facility for Kinetic Analysis (University of Washington, Center for Bioengineering, Seattle, WA). The two-compartment (luminal) model used to simulate targeting of hematologically distributed micrometastases is depicted in Figure 1A. Compartment 1 represents unbound antibody (Ab). Compartment 2 represents antigen-bound antibody (AbAg).

Micrometastases on the Extravascular Side of the Basement Membrane. The three-compartment (extravascular) model used to simulate antibody kinetics when targeting micrometastases on the extravascular side of the capillary basement membrane is depicted in Figure 1B. Compartments 1 and 3 in this model correspond to compartments 1 and 2, respectively, of the luminal model (Fig. 1A). The same antigen concentration and initial

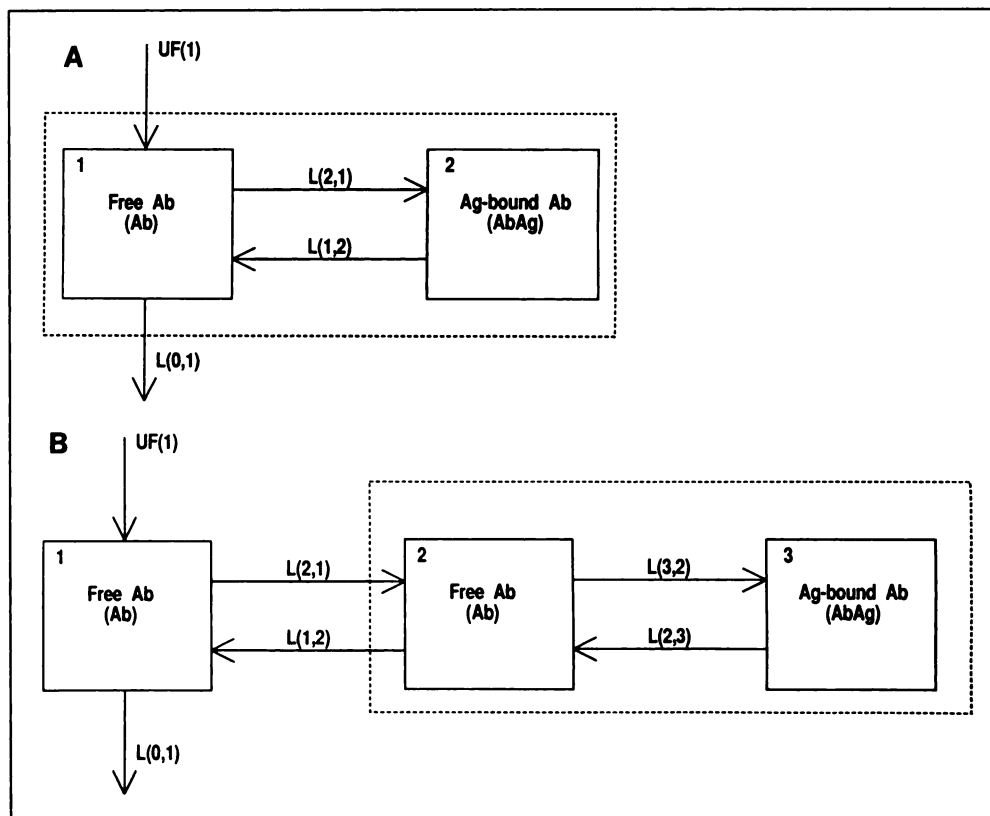


FIGURE 1. (A) Luminal model. The compartmental model employed when simulating antibody targeting to micrometastases on the luminal side of the basement membrane. UF(1) represents the intravenous infusion rate of antibody. $L(2,1)$ is the time-dependent rate at which antibody is bound to antigen. It is equal to $\frac{k_+}{V_d} \cdot (Ag_0 - AbAg)$. $L(1,2)$, the AbAg dissociation rate is equal to k_- . $L(0,1)$ is the clearance rate of antibody from compartment 1. Its value is increased during plasmapheresis. The dotted line represents the 3.8 liter volume within which the tumor cells are distributed. (B) Extravascular model. The compartmental model employed when simulating antibody targeting to micrometastases on the extravascular side of the basement membrane. $L(2,1)$ and $L(1,2)$ are the forward and reverse vascular-to-interstitial space antibody transfer rate constants, respectively. $L(3,2)$ and $L(2,3)$ are defined, respectively, as in $L(2,1)$ and $L(1,2)$ of (A).

volume of antibody distribution are maintained in both models. Movement of antibody from compartment 1 to 2 in this model represents transfer of unbound antibody from the vascular compartment, across the capillary basement membrane to the interstitial fluid volume. Movement of antibody from compartment 2 to 3 is analogous to the transfer of antibody from compartments 1 to 2 in the luminal model and represents a change in state rather than transport to a distinct volume.

Microscopic Model

A 200 μm diameter spherical cluster of tumor cells is assumed lodged on the luminal or extravascular side of the vascular basement membrane. The cell cluster is exposed to an external free antibody concentration that varies with time according to the simulated kinetics of compartments 1 or 2 of the luminal or extravascular macroscopic models, respectively. Antibody penetration into and effusion out of the cell cluster occurs by diffusion. Given the cluster's small dimensions, internal pressure gradients that would lead to convective movement of antibody are negligible. Within the cell cluster, the antibody may bind to and dissociate from a finite number of uniformly distributed antigen sites. Changes in the external concentration of antibody arising from antibody penetration into or effusion out of the cell cluster are assumed negligible. This assumption is justified since the external volume within which the antibody is distributed (3.8 liters) is much greater than the cell cluster (10^{-9} liters).

The coupled partial differential equations with the accompanying boundary and initial conditions are depicted in the Appendix. These were solved numerically using the Schmidt forward finite difference scheme (44) implemented in a FORTRAN program executed on a VAX 8810 computer.

Parameter Values

The parameter values used in the macroscopic and microscopic model simulations are representative values obtained by an extensive search through the pertinent literature. All parameters are for intact antibodies rather than fragments. $L(0,1)$ was obtained by taking the average of several reported values (13,18,45-53). Estimates obtained following human anti-mouse induction or for antibodies known to cross-react with circulating cells were excluded. The association and dissociation rates (k_+ and k_- , respectively) were also obtained by taking the average of reported values. Due to the scarcity of reported measurements at physiological temperature, measurements performed at 37°C (54,55) were combined with values at 4°C (56,57). The number of antigen sites per cell was taken as the mean of the values reported in References 58-65. In both models, total antigen content, A_{g0} , was obtained by multiplying the tumor burden (10 g) by the number of antigen sites per cell. The antigen concentration ($[A_{g0}]$) within the cell cluster was obtained by assuming 10^9 cells per gram (39). The amount of antibody administered and its rate of infusion were chosen to be consistent with published radioimmunotherapy studies (9,12,66,67). In vivo estimates of the antibody diffusion rate constant were obtained from Reference 68. The extravasation and intravasation rates ($L(2,1)$ and $L(1,2)$, respectively) for the extravascular model were obtained by averaging the model-derived estimates of References 45 and 69. To allow intercomparison between the luminal and extravascular models, the distribution volume of antibody in the interstitial space (compartments 2 and 3) was set equal to the vascular volume of the luminal compartment. Table 1 lists the parameters used in the luminal model baseline simulation and in the extra-

TABLE 1
Simulation Parameters

Parameter	Value	
	Baseline, luminal model	Extravascular model
UF(1): Ab (nmole),	66.7	500
Infusion time (h)	1	1
A_{g0} (nmole)	7.5	7.5
$[A_{g0}]$ (nmole l ⁻¹)	1500	1500
V_d (l)	3.8	3.8
k_+ (l nmole ⁻¹ h ⁻¹)	1.3	1.3
k_- (h ⁻¹)	0.3	0.3
D (μm^2 h ⁻¹)	2268	2268
$L(0, 1)$ (h ⁻¹)	0.02	0.02
$L(2, 1)^*$	—	0.1 h ⁻¹
$L(1, 2)$ (h ⁻¹)*	0.3	0.06
R (μm)	100	100

* $L(2,1)$ and $L(1,2)$ in the luminal model represent the antibody-antigen binding parameters; in the extravascular model they represent the extra- and intravasation rates, respectively.

vascular model simulation. Simulations were limited to a 24-hr period since the advantages of plasmapheresis when targeting directly accessible tumor cells would be evident over this time scale. At later times, significant antibody extravasation would limit the effectiveness of plasmapheresis.

Dosimetry

Red Marrow. The mean absorbed dose to the red marrow was calculated according to the Society of Nuclear Medicine, Medical Internal Radionuclide Dosimetry (MIRD) Committee formalism (70-72). The cumulated radioactivity for each compartment of both macroscopic models was obtained by multiplying the contents of each compartment as a function of time by the radiolabeled antibody specific activity and by an exponential decay term corresponding to the half-life of each radionuclide considered. The SAAM UF function was then used to integrate the resulting time-activity curves (73). Five and eight-tenths percent (=0.22 l/3.8 l) of the cumulated activity of compartment 1 in both models was apportioned to the bone marrow. Implicit in such volume-based apportionment is the assumption that the activity concentration in plasma is equal to that in the extracellular fluid of bone marrow (74). Although such an assumption may lead to an overestimate of the bone marrow absorbed dose (75), for purposes of evaluating the utility of plasmapheresis the more conservative assumption was chosen. All of the cumulated activity in compartment 2 of the luminal model was also assigned to marrow. This assumes, conservatively, that all of the tumor cells are localized within the marrow. The unassigned cumulated activity in compartment 1 of both models and in compartments two and three of the extravascular model was assumed to be uniformly distributed throughout the body. The absorbed dose to the bone marrow was obtained as follows:

Luminal Compartmental Model:

$$D_{RM} = (0.058 \cdot \tilde{A}_I + \tilde{A}_{II}) \cdot S_{RM-RM} + 0.942 \cdot \tilde{A}_I \cdot S_{RM-TB} \quad \text{Eq. 1}$$

Extravascular Compartmental Model:

$$D_{RM} = 0.058 \cdot \tilde{A}_I \cdot S_{RM-RM} + (0.942 \cdot \tilde{A}_I + \tilde{A}_{II} + \tilde{A}_{III}) \cdot S_{RM-TB} \quad \text{Eq. 2}$$

where D_{RM} = mean absorbed dose to the red marrow (Gy); \tilde{A}_J = cumulated activity in compartment J (Bq s); S_{RM-RM} = red marrow to red marrow S-factor (Gy Bq⁻¹ s⁻¹); and S_{RM-TB} = total body to red marrow S-factor (Gy Bq⁻¹ s⁻¹).

The S-factors are defined as the “mean absorbed dose to a target organ per unit cumulated activity in the source organ” (72). S-factor values for ¹²³I, ¹²⁵I and ¹³¹I and for a variety of source and target tissue combinations (including red marrow and total body) are tabulated in MIRD Pamphlet No. 11, Revised (72).

Cell Cluster

To obtain the spatial variation of cumulated activity within the cell cluster, the sphere was subdivided into an inner, middle, and outer shell (shells 1, 2 and 3, respectively). The total amount of antibody inside each shell, as a function of time postinjection, was obtained by integrating over each shell volume the free and bound antibody concentration profile obtained from the solution to Equations A1 and A2 (in the Appendix). The results were then integrated over time to give the cumulated activity for each shell (see Appendix).

Using the cumulated activity estimates, the absorbed dose contribution from activity in each shell and from the cluster exterior was individually calculated and then summed to provide the absorbed dose to a given point at a distance, s, from the center of the cell cluster. The cell cluster absorbed dose profile was obtained by calculating the total absorbed dose to a discrete set of points starting at the sphere center and projecting radially outward. The cumulated activity concentration in the cluster exterior was set equal to the cumulated activity concentration of compartments 1 or 2 of the luminal or extravascular models, respectively (see Appendix).

Tabulated point kernels for ¹²³I, ¹²⁵I and ¹³¹I, along with the respective X_{90} values were obtained from Dr. Douglas Simpkin (personal communication). (X_{90} is the radius of a sphere containing 90% of the energy emitted by a point source at the center. A point kernel is a table of values or a mathematical expression that provides the absorbed dose per disintegration a given distance, r, from a point source emitter.) The point kernel for ¹³¹I has been previously published (76). The point kernels for ¹²³I and ¹²⁵I were calculated using a computer code that performs a spectrum-weighted interpolation of monoenergetic electron point kernels to yield a radionuclide point-kernel (76). The monoenergetic electron point kernels used for these calculations are the latest kernels of Berger (Simpkin D, Berger M, *personal communication*) that have been generated using the 1990 version of ETRAN (77). Since the minimum point kernel electron energy tabulated therein is 10 keV, the point kernel for a 1 keV monoenergetic electron emitter included in Berger’s 1973 tabulation (78) was added to the most recent tabulation for the ¹²³I and ¹²⁵I calculations. Due to the abundance of low energy (<5 keV) as well as intermediate energy (30–150 keV) electron emissions in the decay of ¹²³I and ¹²⁵I, the point kernels for these radionuclides were subdivided. “Low” (Klow(r)) and “high” (Khi(r)) energy kernels were used so that the low energy emissions could be applied at an increased (sub-micron) spatial resolution without unnecessarily applying the finer resolution to the higher energy

emissions. Since ¹³¹I does not exhibit such low-energy emissions, a single kernel was used in the absorbed dose calculations (i.e., $Khi(r) = Klow(r)$ in Equation A13 of the Appendix). The photon absorbed dose contribution to the cell cluster was not considered since this is less than 0.1% of the electron absorbed dose.

As indicated in Equations A9 and A11 of the Appendix, the absorbed dose contribution from activity outside the cell cluster was included in the absorbed dose profile calculation. This was accomplished by calculating the absorbed dose to points within the cell cluster arising from activity inside a concentric spherical shell of inner radius R and thickness $2 \cdot X_{90}$ (Equation A11). Contributions to the absorbed dose from emissions beyond twice the X_{90} range for each radionuclide contribute less than 0.1% of the total absorbed dose and were thereby ignored.

To evaluate the contribution of low energy emissions to the cell cluster absorbed dose profile, the absorbed dose ($D_{local}(s)$) to each discrete point in the dose profile curve from activity within a 1 μm radius sphere centered at each point was calculated as shown in the Appendix.

The integrals pertaining to the cell cluster absorbed dose calculation (Equations A6, A7, A10, A11 and A14 of the Appendix) were solved numerically on a PC-compatible, 386/25 computer (Gateway 2000, North Sioux City, SD) using Mathcad 3.0 (MathSoft Inc., Cambridge, MA), a commercially available software package.

Table 2 lists the radionuclide-specific parameters used in performing the dosimetry calculations.

RESULTS

Baseline Simulation

The plasma clearance curve obtained from the luminal compartmental model simulation using the baseline parameters listed in Table 1 is depicted in Figure 2A. The resulting free and antigen-bound antibody concentration profiles within the cell cluster are depicted in Figures 2B–C, respectively. Even though the model provides for direct access of intravenously administered antibody to the tumor cell cluster, a binding-site barrier is still observed over a 24-hr period.

The mean absorbed doses to the red marrow from ¹²³I, ¹²⁵I and ¹³¹I arising from the baseline simulation are shown in Figure 3. The absorbed dose profile across the cell cluster for each radionuclide is depicted in Figures 4A through C. Recalling that the cumulated activity inside the cell cluster was apportioned to three shells of equal thickness (an inner, middle and outer shell), we see, depicted in these figures, the effect of a nonuniform distribution of activity

TABLE 2
Dosimetrical Parameters

Parameter	¹²³ I	¹²⁵ I	¹³¹ I
SA (Bq nmole ⁻¹)	2.2 × 10 ⁸	5.5 × 10 ⁷	5.5 × 10 ⁷
λ _p (h ⁻¹)	5.25 × 10 ⁻²	4.8 × 10 ⁻⁴	3.6 × 10 ⁻³
X ₉₀ (μm)	180	12	830
S _{RM-RM} (Gy Bq ⁻¹ s ⁻¹)*	4.1 × 10 ⁻¹⁵	3.3 × 10 ⁻¹⁵	1.7 × 10 ⁻¹⁴
S _{RM-TB} (Gy Bq ⁻¹ s ⁻¹)*	3.3 × 10 ⁻¹⁶	2.0 × 10 ⁻¹⁶	8.3 × 10 ⁻¹⁶

* From reference 72.

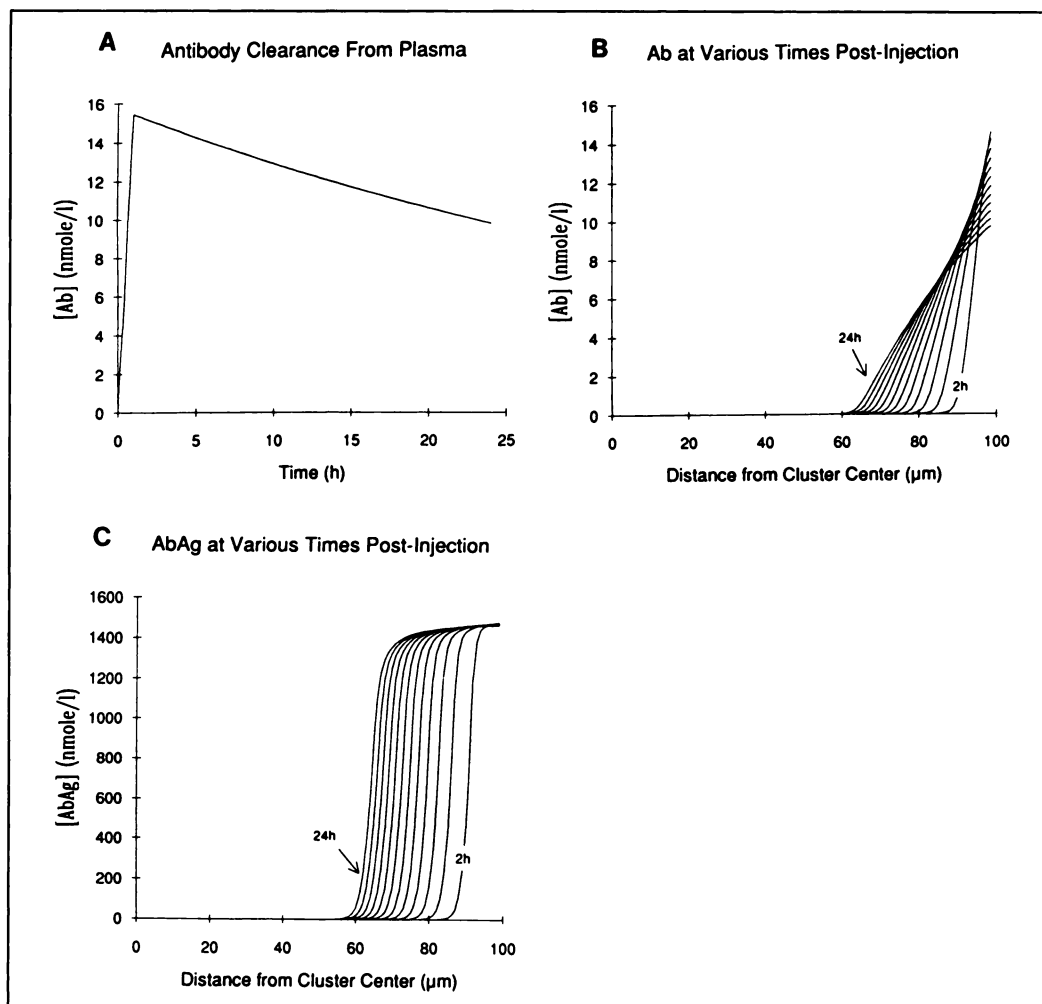


FIGURE 2. Baseline simulation. (A) Free antibody clearance from "plasma" ("plasma" = plasma volume + extracellular fluid volume of liver, spleen and red marrow) obtained by computer simulation of the compartmental model depicted in Figure 1A using the parameters shown in Table 1. Antibody infusion during the first hour is shown as a steep increase in the concentration of antibody. This is followed by a gradual decline resulting from loss due to antigen binding, extravasation and excretion. (B) Free antibody concentration profile inside the cell cluster at various times postinjection. As indicated on the figure, the extreme right and left curves represent the concentration profile at 2 and 24 hr, respectively. Starting at the right the remaining curves were obtained every 2 hr (i.e., at 4, 6, 8, . . . , 22). (C) Corresponding concentration profile for antigen-bound antibody.

on the absorbed dose profiles across the cell cluster. The most striking feature of these curves is the contrast in shape with each radionuclide. Such contrast within a relatively small, 100 μm radius cell cluster, exposes the importance of matching the radionuclide to the expected tumor geometry that one is targeting. The individual contribution to the total absorbed dose from each shell of activity and the contribution due to activity in the exterior are also depicted in Figures 4A–C. The contributions arising from shell 2 and from the exterior are evident in the lower panel of each figure. By examining the "local" absorbed dose profile for each radionuclide one may come to several qualitative conclusions regarding the importance of subcellular antibody localizations as well as tumor cell geometry. As seen on Figure 4B, approximately 50% of the absorbed dose to a given point from ^{125}I arises from

activity within a 1- μm radius sphere around the given point. One may expect, therefore, for cell surface-localized antigen, that greater than 50% of the total absorbed dose depicted will not be delivered to the nucleus of a tumor cell whose radius exceeds the nuclear radius by more than 1 μm . If, on the other hand, the nuclear radius is approximately equal to the cell radius or if the antibody-antigen complex is internalized near the cell nucleus, then the total absorbed dose profile depicted in Figure 4B may reflect the nuclear absorbed dose. Similar observations may be made for ^{123}I in which approximately one-third of the total absorbed dose is from "local" contributions. Such subcellular antibody localization or tumor cell geometry concerns are irrelevant to ^{131}I since the local absorbed dose forms a negligible portion of the total absorbed dose profile (Fig. 4C).

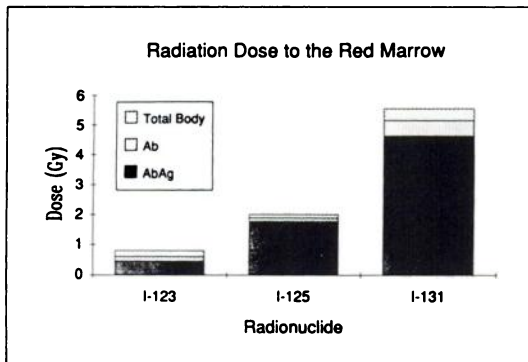


FIGURE 3. Baseline simulation. Absorbed dose to the red marrow from ^{123}I , ^{125}I , and ^{131}I . The absorbed dose contribution from free antibody distributed uniformly throughout the total body ("Total Body") from free antibody in the red marrow ("Ab") and from antigen-bound antibody ("AbAg") is depicted.

Plasmapheresis Simulations

Luminal Model. Table 3 lists the parameter values for each of the luminal model plasmapheresis simulations. The plasmapheresis rates chosen are consistent with clinically available rates (28,29,79,80). Model parameters not shown on this table were maintained at baseline values. The results of simulation 1a are depicted in Figures 5 through 7. Figure 5A shows the rapid rise in plasma

antibody concentration during the 2-hr infusion, followed by a 1 hr waiting period and then by 4 hr of plasmapheresis. Figures 5B and C depict the dramatically improved free and antigen-bound antibody spatial distribution within the cell cluster. As expected, the time-history of free antibody at the cluster surface follows the concentration in plasma (Figs. 5B and 5A, respectively). Accordingly, a large drop, corresponding to the plasmapheresis-induced drop in plasma, is observed at the cluster surface between 2 and 8 hr. The spatial distribution of antibody beyond 8 hr exhibits a slow, uniform drop with time, reflecting the baseline clearance rate of antibody from plasma. Figure 5C demonstrates penetration of the binding-site barrier, yielding a uniform distribution of labeled antibody throughout the cell cluster by 8 hr postinjection. Of particular interest is the observation that essentially full saturation of antigen sites is achieved by 8 hr even though the concentration of free antibody remained at least a factor of 6 below the initial concentration of available antigen sites (i.e., 1500 versus a maximum of 250 nmole/liter). This clearly demonstrates that one need not match the initial concentration of antigen sites in a tumor cell cluster to overcome the binding-site barrier. The absorbed dose to the red marrow from simulation 1a is depicted in Figure 6. Recalling that the specific activity of each radiolabeled antibody was maintained at the baseline value even though the admin-

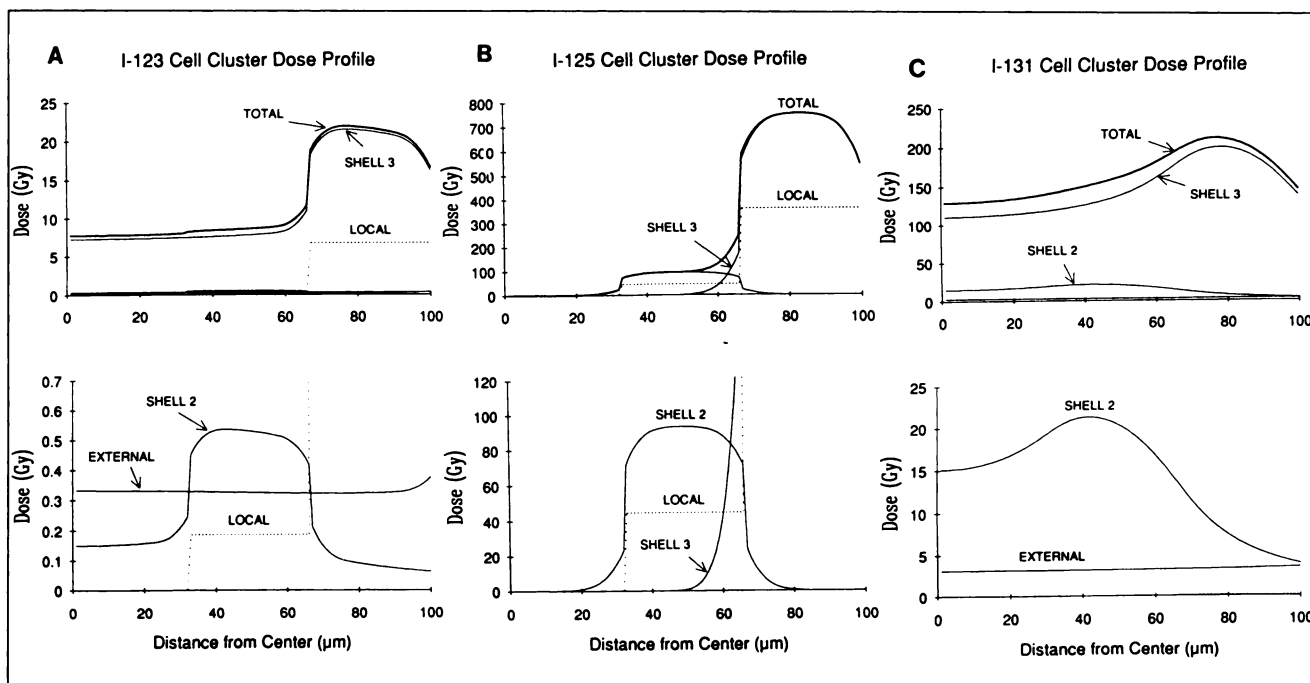


FIGURE 4. Baseline simulation. Absorbed dose profile across the cell cluster for ^{123}I , ^{125}I , and ^{131}I (A, B and C, respectively). The individual contribution to the total absorbed dose from each shell and from the exterior is depicted by the solid lines. The absorbed dose to each point arising from activity within a $1\text{-}\mu\text{m}$ radius sphere about each point (i.e., the "local" absorbed dose) is depicted by the dotted line. The local absorbed dose is shown for comparison, it is already included in each of the solid lines, and does not make up the total absorbed dose sum in these figures. The lower panel of each figure shows, in expanded scale, the absorbed dose contribution from the exterior and from shell 2. In each case, the absorbed dose arising from activity in shell 1 is not shown since it is below the expanded scale (i.e., approximately zero). Likewise, the external absorbed dose in B and the local dose in C is not shown, since in each case, the absorbed dose is below the expanded scale of the lower panel.

TABLE 3
Luminal Model Plasmapheresis Simulation Parameters

Parameter	Simulation number			
	1a	1b	2a	2b
Ab administered (nmole), infusion time (h)	1000, 2	1000, 2	500, 1	500, 1
Plasmapheresis rate (h^{-1})	0.275	0.403	0.275	0.275
Plasmapheresis onset time, duration (h)	3, 4	3, 4	2, 4	3, 4

istered amount of antibody was increased 15-fold, we obtain an increase in red marrow absorbed dose that ranges from slightly above 2-fold to approximately 4-fold above baseline for ^{123}I and ^{125}I , respectively. In each case the increase is attributable to free antibody in the marrow and in the total body. Figure 7 depicts the total absorbed dose profile across the cell cluster for each radionuclide. In contrast to the curves depicted in Figure 4, a relatively uniform distribution of absorbed dose throughout the cell cluster is achieved for all three radionuclides. The therapeutic ratio (i.e., cell cluster dose at center divided by the mean red marrow dose) is 10, 225, and 35 for ^{123}I , ^{125}I and ^{131}I , respectively. This compares with 8, ≈ 0 , and 23 for the corresponding baseline simulations.

The effect of increasing the plasmapheresis rate 1.5-fold is examined in simulation 1b. The increased plasmapheresis rate leads to an 80% decrease in plasma antibody concentration (not shown). This may be compared to the 70% decrease achieved when plasmapheresis is applied at the rate of simulation 1a (Fig. 5A). A 50% increase in the rate of plasmapheresis, therefore, has resulted in a 10% gain in plasma clearance. The more rapid drop in plasma antibody concentration leads to a 2-hr delay in antigen-site saturation across the cell cluster (not shown). Despite this delay, the absorbed dose profile across the cell cluster (not shown) is essentially identical to that depicted in Figure 7. The gain in therapeutic ratio as a result of

increasing plasma clearance of free antibody without affecting the cell cluster absorbed dose profile is depicted in Figure 8. Also shown in this figure is the therapeutic ratio obtained for each radionuclide under the conditions of simulation 1 when plasmapheresis was not instituted. The clear advantage of ^{125}I over the other two radionuclides for radioimmunotherapy under the specific conditions of simulation 1 is strikingly evident. Although a 2-fold increase in the therapeutic ratio is obtained by performing plasmapheresis with this radionuclide, the therapeutic ratio obtained by administering a large amount of radiolabeled antibody (i.e., simulation 1) without instituting plasmapheresis is still adequate for radioimmunotherapy. The therapeutic ratio for ^{131}I with accelerated plasmapheresis is 46. Assuming 2.5 Gy is the maximum tolerable absorbed dose to the red marrow (74), this translates into an absorbed dose of 115 Gy to the cell cluster. The corresponding absorbed dose without plasmapheresis would be 53 Gy. In this particular example, therefore, the use of plasmapheresis yields a highly significant increase in the tumor cell kill probability (81,82). Despite its significant particulate emissions and largely due to its short half-life, ^{123}I does not yield an adequate therapeutic ratio for radioimmunotherapy under the particular conditions of simulation 1.

Simulations 2a and 2b illustrate the sensitivity of the proposed plasmapheresis technique to the total amount of

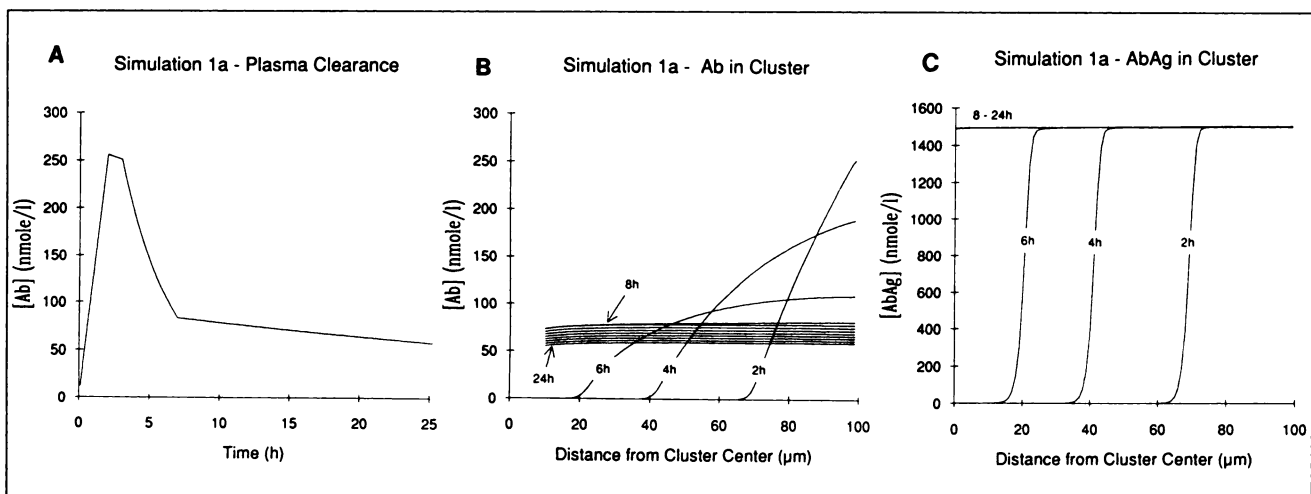


FIGURE 5. Simulation 1a. (A) Free antibody clearance from plasma. The effect of plasmapheresis may be seen in the rapid drop in antibody concentration from 3 to 7 hr postinjection. (B) Free and (C) bound antibody concentration profile inside the cell cluster at various times postinjection.

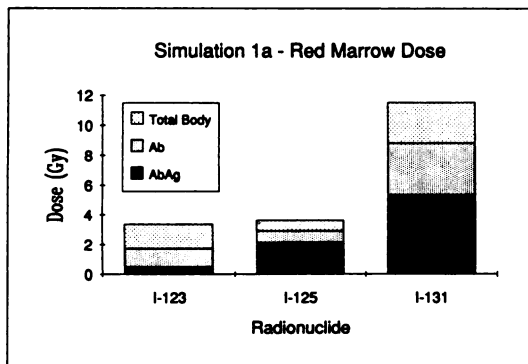


FIGURE 6. Simulation 1a. Absorbed dose to the red marrow from ^{123}I , ^{125}I and ^{131}I . Shaded regions are defined as in Figure 3.

administered antibody. Simulation 2a differs from 1a in that 500 nmole of antibody are administered over 1 hr rather than 1000 over 2 hr. Simulation 2b examines the effect of increasing the waiting period following the end of antibody infusion to 2 hr from 1 hr. The spatial distribution of antibody arising from simulation 2a lies between that obtained from simulation 1a and the baseline simulation. Halving the total administered antibody leads to a

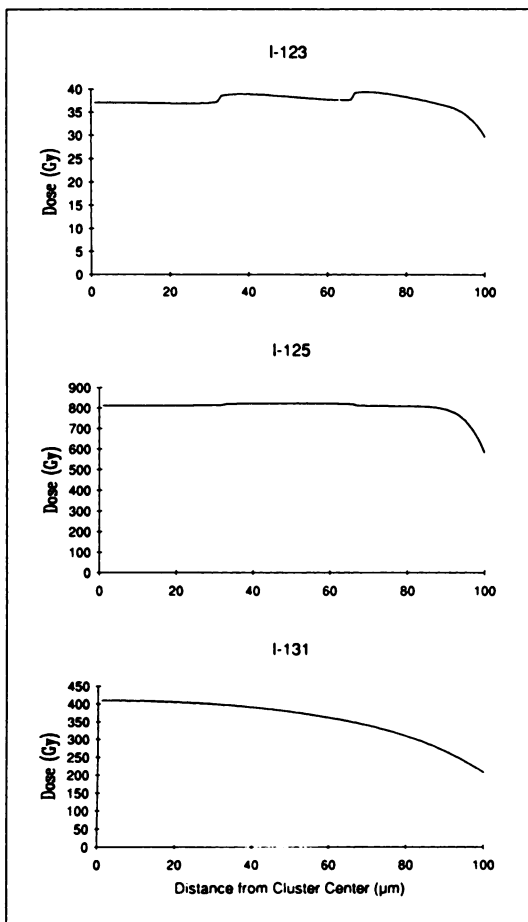


FIGURE 7. Simulation 1a. Total absorbed dose profile across the cell cluster for ^{123}I , ^{125}I and ^{131}I .

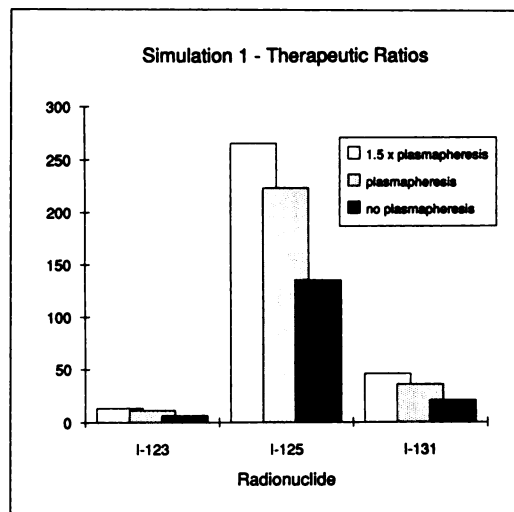


FIGURE 8. Simulation 1. The therapeutic ratios (=absorbed dose at cell cluster center + red marrow absorbed dose) resulting from simulation 1b ("1.5 × plasmapheresis," unfilled bar), simulation 1a ("plasmapheresis," light grey bar) and the input parameters of simulations 1a or b without plasmapheresis ("no plasmapheresis," dark grey bar).

24-hr delay in achieving a uniform distribution of antibody within the cell cluster. The effect of this on the cell cluster absorbed dose profile is most pronounced for ^{123}I which exhibits a 40% drop in delivered absorbed dose (relative to Fig. 7) at the center. The effect on the longer-lived radionuclides, ^{125}I and ^{131}I , is barely detectable (data not shown). The therapeutic ratios for simulation 2a are 10, 290, and 48 for ^{123}I , ^{125}I and ^{131}I , respectively. The ratios for ^{125}I and ^{131}I surpass those obtained for simulation 1b in which antibody uniformity within the cell cluster was achieved by 8 hr postinjection. Since simulation 2a yielded a slightly lower absorbed dose at the cell cluster center for these two radionuclides, relative to the absorbed dose obtained from simulation 1, the improvement in therapeutic ratio is the result of a decrease in the red marrow absorbed dose.

The results obtained with simulation 2b, in which the waiting period after the end of infusion is increased to 2 hr are not significantly different from those obtained from simulation 2a (data not shown).

Extravascular Model

The compartmental model depicted in Figure 1B was used to examine the feasibility of using plasmapheresis to enhance the therapeutic ratio when targeting micrometastatic disease on the extravascular side of the vascular basement membrane. Figures 9A–B depict the free and bound antibody concentration inside the cell cluster. Although the results are better than those obtained in the baseline simulation (Figs. 2B,C), a core of unlabeled cells remains. The resulting absorbed dose profiles are depicted in Figure 10. The corresponding therapeutic ratios along with the ratios obtained for earlier simulations are listed

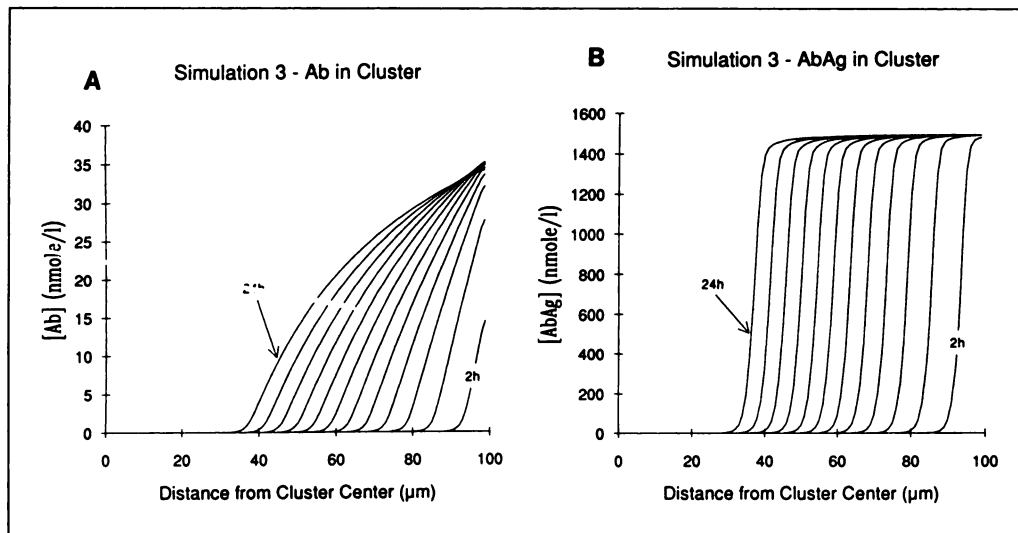


FIGURE 9. Simulation 3. Free (A) and bound (B) antibody concentration profile inside the cell cluster at various times postinjection.

in Table 4. Due to its long range emissions and to the decrease in red marrow absorbed dose resulting from the assumed absence of antigen-positive cells in marrow (i.e., the extravascular model), ^{131}I exhibits a therapeutic ratio

that is still adequate for successful radioimmunotherapy of 200- μm diameter cell clusters.

DISCUSSION

Mathematical modeling analysis of both the macro- and microdistribution of radiolabeled antibody has provided information that may help guide and evaluate future treatment strategies using radiolabeled antibodies. Compartmental modeling approaches have provided information regarding: antibody administration strategies for improving radioimmunodiagnosis and radioimmunotherapy (45, 69,83-85); the differences in biodistribution, catabolism and excretion between IgG, $\text{F}(\text{ab}')_2$, and Fab' antibody (11); the effect of circulating antigen on antibody biodistribution (86); and the interrelationship between antibody size, affinity and protein binding on tumor uptake (8). Mathematical analyses which combine simulations of the macroscopic distribution of antibody with regional or microscopic simulations have demonstrated the significance of blood vessel permeability, antibody diffusion and convection, and antibody-antigen binding parameters in targeting extravascular tumor (30-33,87,88). A key finding of these works has been the prediction of a "binding-site" barrier to antibody penetration of tumor (30-33) that has been observed experimentally (89-91).

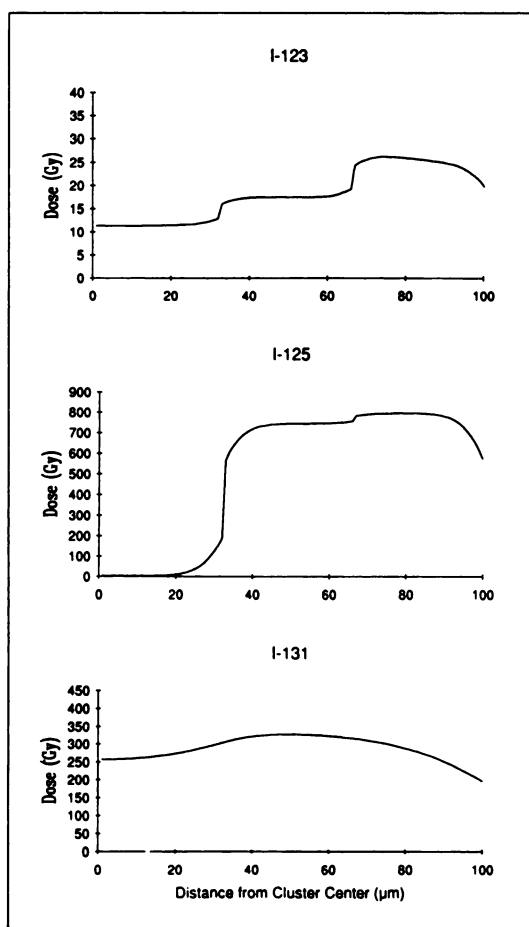


FIGURE 10. Simulation 3. Total absorbed dose profile across the cell cluster for ^{123}I , ^{125}I and ^{131}I . The y-axis scale for each panel is the same as that in Figure 7.

TABLE 4
Summary of Therapeutic Ratios*

Radionuclide	Simulation number					
	Baseline	1a	1b	2a	2b	3
^{123}I	8	10	13	12	13	7
^{125}I	0	225	265	291	288	2
^{131}I	23	35	46	48	48	44

* Therapeutic ratio = absorbed dose to cell cluster center + absorbed dose to red marrow.

This work evaluates the utility of plasmapheresis in improving antibody targeting of pre-vascularized, hematologically distributed micrometastases. A mathematical model of antibody penetration into a 200- μm diameter cell cluster exposed to a time-varying external concentration of antibody has been used to investigate the influence of plasmapheresis on the spatial distribution of antibody within the cell cluster and on the resulting absorbed dose profile across the cell cluster. Consistent with the work of Fujimori et al. which demonstrated the binding-site barrier for extravascular tumors (30–33), the results demonstrate that a “typical” radioimmunotherapy protocol (i.e., 10 mg of antibody infused over 1 hr—the “baseline” simulation) yields a highly nonuniform distribution of antibody inside a cell cluster located within the vasculature (i.e., on the luminal side of the basement membrane). Depending on the radionuclide employed, this translates into an absorbed dose profile that ranges from marginally acceptable (as in ^{131}I) to one that produces no absorbed dose to the central portion of the cell cluster (as in ^{125}I). In all cases the resulting red marrow absorbed dose yields a therapeutic ratio at the cluster center that precludes successful eradication of micrometastatic disease without prohibitive red marrow damage. By administering approximately 8-fold more antibody (i.e., 75 mg infused over 1 hr—simulation 2), the spatial distribution of antibody inside the cell cluster is dramatically improved such that by 24 hr, a uniform distribution is achieved. The resulting red marrow absorbed dose may be reduced sufficiently with plasmapheresis to yield therapeutic ratios for ^{125}I and ^{131}I that could lead to successful radioimmunotherapy of micrometastases without prohibitive red marrow damage. The foregoing discussion applies only to micrometastases that are located on the luminal side of the vascular basement membrane and that are, therefore, rapidly accessible to intravenously administered antibody. The plasmapheresis technique (as implemented for targeting hematologically distributed micrometastases) is significantly compromised when one is targeting disease on the extravascular side of the basement membrane. The results show that an approximate 8-fold increase in intravenously administered antibody is not reflected in the interstitial space antibody concentration and as a result leads to incomplete penetration of the cell cluster over the simulation time investigated.

It is important to point out several caveats in applying the results herein reported. Although the simulations suggest that ^{125}I would be ideal in radioimmunotherapy of hematologically distributed micrometastases when the protocol of simulations 1 or 2 is employed, considerations not included in the model must also be weighed. Since ^{125}I has a long half-life, one should expect that a substantial fraction of the radionuclide will cross the basement membrane of most tissues. Cross-reactivity of the radiolabeled antibody with normal tissue could lead to unacceptably high absorbed doses to these tissues. In general, if the

radionuclide exhibits a long half-life (i.e., greater than the half-life of antibody penetration across the vascular basement membrane), cross-reactivity concerns become paramount. In contrast, these concerns are minimal with ^{123}I since by the time the antibody has crossed the basement membrane of most normal tissues a large fraction of the radionuclide has already decayed. (Cross-reactivity with liver, spleen and red marrow is always of concern because of the undeveloped basement membrane in these tissues.) The long half-life of ^{125}I also raises dose rate concerns. The relatively low dose rate of this radionuclide may diminish its effectiveness in eradicating rapidly proliferating tumor cells (81). It is also important to note that all of the simulations were performed for a 200 μm diameter cell cluster. Although there is evidence that prevascularized, hematologically distributed micrometastases do not reach the dimensions achieved by in vitro grown spheroids (92, 93), a detailed assessment of the in vivo size distribution of micrometastases is lacking. Since the very large therapeutic ratio of ^{125}I is extremely sensitive to antibody uniformity inside each cell cluster, the presence of significantly larger cell clusters is likely to lead to treatment failure if ^{125}I is used. Furthermore, when uniformity is achieved, significant cell kill will only occur if the antibody-antigen complex is internalized (94). It is important to note that estimation of the absorbed dose to the cell nucleus or to DNA from an internalized Auger emitter may (depending upon the dose rate and the volume chosen for the calculation) require a microdosimetric treatment rather than the mean absorbed dose calculation that is provided by the conventional MIRD formalism.

Plasmapheresis is, perhaps, the most direct implementation of a general strategy designed to overcome the binding site barrier. The essence of such a strategy is to expose the tumor cluster to a very high antibody concentration long enough to overcome the binding site barrier. Excess antibody is then rapidly removed so as to reduce the red marrow absorbed dose. One alternative to the use of plasmapheresis for this purpose is what may be characterized as a “chaser” approach (15–17,95). In such an approach, an infusion of radiolabeled antibody is followed by unlabeled (cold) antibody that is specific to the F_c region of the previously administered (labeled) antibody. The cold antibody binds to the labeled antibody presumably without affecting its binding capacity to tumor-associated antigen (i.e., the variable regions are not affected). Free labeled Ab, however, would complex with the chaser and presumably clear at a much faster rate. In analogy to plasmapheresis, this approach strives to clear the body of excess antibody.

In conclusion, administration of a high concentration of radiolabeled antibody followed by plasmapheresis is shown to yield a considerable improvement in the therapeutic ratio for hematologically distributed micrometastases. When this strategy is applied to micrometastases on the extravascular side of the basement membrane, no

substantial improvement is observed for the two shorter-range emitters (^{123}I and ^{125}I) examined; for a relatively long-range emitter such as ^{131}I the therapeutic ratio is improved.

APPENDIX

Microscopic Model Equations

$$\frac{\partial[\text{Ab}(r, t)]}{\partial t} = D \left(\frac{\partial^2[\text{Ab}(r, t)]}{\partial r^2} + \frac{2}{r} \frac{\partial[\text{Ab}(r, t)]}{\partial r} \right) - k_+([\text{Ag}_0] - [\text{AbAg}(r, t)])([\text{Ab}(r, t)]) + k_-([\text{AbAg}(r, t)]) \quad \text{Eq. A1}$$

$$\frac{\partial[\text{AbAg}(r, t)]}{\partial t} = k_+([\text{Ag}_0] - [\text{AbAg}(r, t)])([\text{Ab}(r, t)]) - k_-([\text{AbAg}(r, t)]) \quad \text{Eq. A2}$$

$$[\text{Ab}(r, t)] = P(t) \quad \text{for } r > R, \text{ for all } t \quad \text{Eq. A3}$$

$$[\text{Ab}(r, t)] = 0 \quad \text{for } r \leq R, t = 0 \quad \text{Eq. A4}$$

$$[\text{AbAg}(r, t)] = 0 \quad \text{for all } r, t = 0 \quad \text{Eq. A5}$$

where

$[\text{Ab}(r, t)]$ = free antibody conc. at r from the center and at time t (nmole l^{-1})

$[\text{AbAg}(r, t)]$ = concentration of antigen-bound antibody (nmole l^{-1})

$[\text{Ag}_0]$ = initial concentration of free antigen in the cell cluster (nmole l^{-1})

D = diffusion rate of antibody inside the cell cluster ($\mu\text{m}^2 \text{h}^{-1}$)

k_+ = association rate for antibody-antigen binding (1 nmole $^{-1} \text{h}^{-1}$)

k_- = antibody-antigen dissociation rate constant (h^{-1})

$P(t)$ = free antibody concentration outside the cell cluster (nmole l^{-1})

R = spheroid radius (μm).

Total Antibody in Each Shell as a Function of Time

$$I(t)_i = \int_0^{2\pi} \int_0^\pi \int_{(i-1) \cdot R/3}^{i \cdot R/3} ([\text{Ab}(r, t)] + [\text{AbAg}(r, t)]) \cdot r^2 \cdot \sin(\theta) \cdot \phi \cdot dr \cdot d\theta \cdot d\phi \quad \text{Eq. A6}$$

where $I(t)_i$ = free and bound antibody in shell i (nmole).

The Cumulated Activity Concentration for Each Shell

$$[\tilde{A}]_i = \frac{\int_0^T I(\tau)_i \cdot SA \cdot e^{-\lambda_p \tau} \cdot d\tau + \int_T^\infty I(T)_i \cdot SA \cdot e^{-(\lambda_p + \lambda_B) \tau} \cdot d\tau}{V_i} \quad \text{Eq. A7}$$

$$V_i = \frac{4}{3} \cdot \pi \cdot \left[\left(i \cdot \frac{R}{3} \right)^3 - \left((i-1) \cdot \frac{R}{3} \right)^3 \right] \quad \text{Eq. A8}$$

where

$[\tilde{A}]_i$ = cumulated activity concentration in shell i ($\text{Bq s } \mu\text{m}^{-3}$)

V_i = volume of spherical shell i (μm^3)

SA = specific activity of the radiolabeled antibody (Bq nmole^{-1})

λ_p = radionuclide decay rate (s^{-1})

λ_B = long-term clearance rate of antibody from the cell cluster (= 1.9×10^{-7} , obtained by fitting the result of a 200-hr simulation to a single exponential (s^{-1}))

T = last time postinjection for which $I(t)$ was calculated (excluding the 200 hr simulation performed for estimating λ_B) (s).

Cell Cluster Absorbed Dose Calculations

$$D(s) = D_1(s) + D_2(s) + D_3(s) + D_{\text{ext}}(s) \quad \text{Eq. A9}$$

$$D_1(s) = \int_0^{2\pi} \int_0^\pi \int_{(i-1) \cdot R/3}^{i \cdot R/3} [\tilde{A}]_i \cdot K(q(r, \theta, s)) \cdot r^2 \cdot \sin(\theta) \cdot \phi \cdot dr \cdot d\theta \cdot d\phi \quad \text{Eq. A10}$$

$$D_{\text{ext}}(s) = \int_0^{2\pi} \int_0^\pi \int_R^{2 \cdot X_{90}} [\tilde{A}]_j \cdot K(q(r, \theta, s)) \cdot r^2 \cdot \sin(\theta) \cdot \phi \cdot dr \cdot d\theta \cdot d\phi \quad \text{Eq. A11}$$

$$q(r, \theta, s) = \sqrt{(r \cdot \cos(\theta) - s)^2 + (r \cdot \sin(\theta))^2} \quad \text{Eq. A12}$$

$$K(r) = \begin{cases} K_{\text{low}}(r) & r \leq 1 \mu\text{m} \\ K_{\text{hi}}(r) & r > 1 \mu\text{m} \end{cases} \quad \text{Eq. A13}$$

where

$D_1(s)$ = absorbed dose a distance s from the cell cluster center from shell i (Gy)

$D_{\text{ext}}(s)$ = absorbed dose from activity outside the cell cluster (Gy)

$q(r, \theta, s)$ = distance between a target point at $(s, 0, \phi)$ and a source point at (r, θ, ϕ) (μm)

$K_{\text{low}}(r)$ = dose point-kernel in water for $r \leq 1 \mu\text{m}$ ($\text{Gy Bq}^{-1} \text{s}^{-1}$)

$K_{\text{hi}}(r)$ = dose point-kernel in water for $r > 1 \mu\text{m}$ ($\text{Gy Bq}^{-1} \text{s}^{-1}$)

$[\tilde{A}]_j$ = cumulated activity in compartments 1 or 2 of the luminal or extravascular models, respectively ($\text{Bq s } \mu\text{m}^{-3}$)

X_{90} = radius of a sphere enclosing 90% of the energy emitted by a point source at its center (μm).

Localized Absorbed Dose Calculation

$$D_{\text{local}}(s) = \int_0^{2\pi} \int_0^\pi \int_0^1 [\tilde{A}(s)] \cdot K_{\text{low}}(q(r, \theta, s)) \cdot r^2 \cdot \sin(\theta) \cdot \phi \cdot dr \cdot d\theta \cdot d\phi \quad \text{Eq. A14}$$

$$[\tilde{A}(s)] = \begin{cases} [\tilde{A}]_1 & s \leq 33 \mu\text{m} \\ [\tilde{A}]_2 & 33 < s \leq 67 \mu\text{m} \\ [\tilde{A}]_3 & s \leq 100 \mu\text{m} \end{cases} \quad \text{Eq. A15}$$

ACKNOWLEDGMENTS

The author thanks Dr. Douglas J. Simpkin of the Department of Radiology at St. Luke's Medical Center, Milwaukee, WI, for providing the electron point kernels for ^{123}I , ^{125}I and ^{131}I , and for the helpful suggestions on their use. The comments and suggestions of Mr. Alan Alfieri and Drs. Steven Larson, C. Clifton Ling, David Scheinberg and Alan Weinstein are also appreciated. The author is the recipient of a Cancer Research Institute/Jesselson Foundation Fellowship.

REFERENCES

- Epenetos AA, Snook D, Durbin H, Johnson PM, Taylor-Papadimitriou J. Limitations of radiolabeled monoclonal antibodies for localization of human neoplasms. *Cancer Res* 1986;46:3183-3191.
- Sharkey RM, Blumenthal RD, Hansen HJ, Goldenberg DM. Biological

- considerations for radioimmunotherapy. *Cancer Res* 1990;50(suppl):964s-969s.
3. Order SE, Sleeper AM, Stillwagon GB, Klein JL, Leichner PK. Radiolabeled antibodies: results and potential in cancer therapy. *Cancer Res* 1990;50(suppl):1011s-1013s.
 4. Begent RHJ, Pedley RB. Antibody targeted therapy in cancer: comparison of murine and clinical studies. *Cancer Treat Rev* 1990;17:373-378.
 5. Ward BG, Mather SJ, Hawkins LR, et al. Localization of radioiodine conjugated to the monoclonal antibody HMFG2 in human ovarian carcinoma: assessment of intravenous and intraperitoneal routes of administration. *Cancer Res* 1987;47:4719-4723.
 6. Lee Y, Bullard DE, Wikstrand CJ, Zalutsky MR, Muhlbaier LH, Bigner DD. Comparison of monoclonal antibody delivery to intracranial glioma xenografts by intravenous and intracarotid administration. *Cancer Res* 1987;47:1941-1946.
 7. Haisma JJ, Moseley KR, Battaile A, Griffiths TC, Knapp RC. Distribution and pharmacokinetics of radiolabeled monoclonal antibody OC 125 after intravenous and intraperitoneal administration in gynecologic tumors. *Am J Obstet Gynecol* 1988;159:843-848.
 8. Thomas GD, Chappell MJ, Dykes PW, et al. Effect of dose, molecular size, affinity, and protein binding on tumor uptake of antibody or ligand: a biomathematical model. *Cancer Res* 1989;49:3290-3296.
 9. Bernstein ID, Eary JF, Badger CC, et al. High dose radiolabeled antibody therapy of lymphoma. *Cancer Res* 1990;50(suppl):1017s-1021s.
 10. Brown BA, Comeau RD, Jones PL, et al. Pharmacokinetics of the monoclonal antibody B72.3 and its fragments labeled with either ¹²⁵I or ¹¹¹In. *Cancer Res* 1987;47:1149-1154.
 11. Covell DG, Barbet J, Holton OD, Black CDV, Parker RJ, Weinstein JN. Pharmacokinetics of monoclonal immunoglobulin G₁, F(ab')₂, and Fab' in mice. *Cancer Res* 1986;46:3969-3978.
 12. Carrasquillo JA, Krohn KA, Beaumier P, et al. Diagnosis of and therapy for solid tumors with radiolabeled antibodies and immune fragments. *Cancer Treat Rep* 1984;68:317-328.
 13. LoBuglio AF, Wheeler RH, Trang J, et al. Mouse/human chimeric monoclonal antibody in man: kinetics and immune response. *Proc Natl Acad Sci USA* 1989;86:4220-4224.
 14. Buchsbaum DJ, Brubaker PG, Hanna DE, et al. Comparative binding and preclinical localization and therapy studies with radiolabeled human chimeric and murine 17-1A monoclonal antibodies. *Cancer Res* 1990;50(suppl):993s-999s.
 15. Sharkey RM, Primus FJ, Goldenberg DM. Second antibody clearance of radiolabeled antibody in cancer radioimmunodetection. *Proc Natl Acad Sci USA* 1984;81:2843-2846.
 16. Goodwin D, Meares C, Diamanti C, et al. Use of specific antibody for rapid clearance of circulating blood background from radiolabeled tumor imaging proteins. *Eur J Nucl Med* 1984;9:209-215.
 17. Wahl RL and Fisher S. Intraperitoneal delivery of monoclonal antibodies: enhanced regional delivery advantage using intravenous unlabeled anti-mouse antibody. *Int J Radiat Appl Instrum, Part B, Nucl Med Biol* 1987;14:611-615.
 18. Rosenblum MG, Maki LM, Murray JL, Carlo DJ, Gutterman JU. Interferon-induced changes in pharmacokinetics and tumor uptake of ¹¹¹In-labeled antimelanoma antibody 96.5 in melanoma patients. *J Natl Cancer Inst* 1988;80:160-165.
 19. DiMaggio JJ, Scheinberg DA, Houghton AN. Monoclonal antibody therapy of cancer. *Cancer Chemotherapy and Biological Response Modifiers Annual* 1990;11:177-203.
 20. Schlom J, Hand PH, Greiner JW, et al. Innovations that influence the pharmacology of monoclonal antibody guided tumor targeting. *Cancer Res* 1990;50(suppl):820s-827s.
 21. Press OW, DeSantes K, Anderson SK, Geissler F. Inhibition of catabolism of radiolabeled antibodies by tumor cells using lysosomotropic amines and carboxylic ionophores. *Cancer Res* 1990;50:1243-1250.
 22. Kalofonos H, Rowlinson G, Epenetos AA. Enhancement of monoclonal antibody uptake in human colon tumor xenografts following irradiation. *Cancer Res* 1990;50:159-163.
 23. Zimmer AM, Rosen ST, Spies SM, et al. Radioimmunotherapy of patients with cutaneous T-cell lymphoma using an iodine-131-labeled monoclonal antibody: analysis of retreatment following plasmapheresis. *J Nucl Med* 1988;29:174-180.
 24. Wahl RL, Piko CR, Beers BA, Geatti O, Johnson J, Sherman P. Systemic perfusion: a method of enhancing relative tumor uptake of radiolabeled monoclonal antibodies. *Int J Radiat Appl Instrum, Part B, Nucl Med Biol* 1988;15:611-616.
 25. Norrgren K, Strand S-E, Nilsson R, Lindgren L, Lillehorn P. Evaluation of extracorporeal immunoabsorption for reduction of the blood background in diagnostic and therapeutic applications of radiolabeled Mabs. *Antibody Immunoconj Radiopharm* 1991;4:907-914.
 26. Hartmann C, Bloedow DC, Dienhart DG, et al. A pharmacokinetic model describing the removal of circulating radiolabeled antibody by extracorporeal immunoabsorption. *J Pharmacol Biopharm* 1991;19(4):385-403.
 27. Norrgren K, Strand S-E, Ingvar C. Contrast enhancement in RII and modification of the therapeutic ratio in RIT: a theoretical evaluation of simulated extracorporeal immunoabsorption. *Antibody Immunoconj Radiopharm* 1992;5:61-73.
 28. Lear JL, Kasliwal RK, Feyerabend AJ, et al. Improved tumor imaging with radiolabeled monoclonal antibodies by plasma clearance of unbound antibody with anti-antibody column. *Radiology* 1991;179:509-512.
 29. DeNardo GL, DeNardo SJ, Lewis JP, et al. Treatment of B cell malignancies in patients using fractionated dose or maximum tolerated dose of I-131 LYM-1 without and with immunophoresis. *J Nucl Med* 1991;32:921.
 30. Fujimori K, Covell DG, Fletcher JE, Weinstein JN. Modeling analysis of the global and microscopic distribution of immunoglobulin G, F(ab')₂, and Fab in tumors. *Cancer Res* 1989;49:5656-5663.
 31. Fujimori K, Covell DG, Fletcher JE, Weinstein JN. A modeling analysis of monoclonal antibody percolation through tumors: a binding-site barrier. *J Nucl Med* 1990;31:1191-1198.
 32. Fujimori K, Fisher DR, Weinstein JN. Integrated microscopic-macroscopic pharmacology of monoclonal antibody radioconjugates: the radiation dose distribution. *Cancer Res* 1991;51:4821-4827.
 33. van Osdol W, Fujimori K, Weinstein JN. An analysis of monoclonal antibody distribution in microscopic tumor nodules: consequences of a "binding site barrier." *Cancer Res* 1991;51:4776-4784.
 34. Butler TP, Grantham FH, Gullino PM. Bulk transfer of fluid in the interstitial compartment of mammary tumors. *Cancer Res* 1975;35:3084-3088.
 35. Jain RK, Baxter LT. Mechanisms of heterogeneous distribution of monoclonal antibodies and other macromolecules in tumors: significance of elevated interstitial pressure. *Cancer Res* 1988;48:7022-7032.
 36. Jain RK. Physiological barriers to delivery of monoclonal antibodies and other macromolecules in tumors. *Cancer Res* 1990;50(suppl):814s-819s.
 37. Yuan F, Baxter LT, Jain RK. Pharmacokinetic analysis of two-step approaches using bifunctional and enzyme-conjugated antibodies. *Cancer Res* 1991;51:3119-3130.
 38. Weiss L, Orr FW, Honn KV. Interactions of cancer cells with the microvasculature during metastasis. *FASEB J* 1988;2:12-21.
 39. Hiddemann W, Clarkson BD, Buchner T, Melamed MR, Andreef M. Bone marrow cell count per cubic millimeter bone marrow: a new parameter for quantitating therapy-induced cytoreduction in acute leukemia. *Blood* 1982;59:216-221.
 40. International Commission on Radiological Protection. *Report of the task group on reference man*. ICRP Publication 23, New York: Pergamon Press; 1975.
 41. Bloom W, Fawcett DW. *A Textbook of histology*, 10th edition. Philadelphia: W.B. Saunders Co.; 1975.
 42. Tavassoli M, Yoffey YM. *Bone marrow: structure and function*. New York: Alan R. Liss; 1983.
 43. Berman M., Weiss MF. *SAAM Manual*. US DHEW Publication No., (NIH) 78-810: Washington; 1978.
 44. Gerald CF, Wheatley PO. *Applied numerical analysis*. Reading, MA: Addison-Wesley Publishing Co.; 1984.
 45. Eger RR, Covell DG, Carrasquillo JA, et al. Kinetic model for the biodistribution of an ¹¹¹In-labeled monoclonal antibody in humans. *Cancer Res* 1987;47:3328-3336.
 46. Harwood SJ, Carroll RG, Webster WB, et al. Human biodistribution of In-111-labeled B72.3 monoclonal antibody. *Cancer Res* 1990;50(suppl):932s-936s.
 47. Kalofonos HP, Sackier JM, Hatzistilianou M, et al. Kinetics, quantitative analysis and radioimmunolocalisation using indium-111-HMFG1 monoclonal antibody in patients with breast cancer. *Br J Cancer* 1989;59:939-942.
 48. Carrasquillo JA, Sugarbaker P, Colcher D, et al. Radioimmunoscinigraphy of colon cancer with iodine-131-labeled B72.3 monoclonal antibody. *J Nucl Med* 1988;29:1022-1030.
 49. Skarlos DV, Malamitsi J, Sivolapenko GB, et al. A preliminary study of brain gliomas with H17E2 monoclonal antibody: immunoscintigraphy and pharmacokinetics. *Int J Biol Markers* 1989;4:135-141.
 50. Rosenblum MG, Murray JL, Lamki L, David G, Carlo D. Comparative clinical pharmacology of In-111-labeled murine monoclonal antibodies. *Cancer Chemother Pharmacol* 1987;20:41-47.

51. Perkins AC, Pimm MV. Differences in tumour and normal tissue concentrations of iodine- and indium-labeled monoclonal antibody I. The effect on image contrast in clinical studies. *Eur J Nucl Med* 1985;11:295-299.
52. Murray JL, Rosenblum MG, Lamki L, et al. Clinical parameters related to optimal tumor localization of indium-111-labeled mouse antimelanoma monoclonal antibody ZME-018. *J Nucl Med* 1987;28:25-33.
53. Hayes DF, Zalutsky MR, Kaplan W, et al. Pharmacokinetics of radiolabeled monoclonal antibody B6.2 in patients with metastatic breast cancer. *Cancer Res* 1986;46:3157-3163.
54. Sheldon K, Marks A, Baumal R. Characterization of binding of four monoclonal antibodies to the human ovarian adenocarcinoma cell line HEY. *Biochem Cell Biol* 1987;65:423-428.
55. Mattes MJ, Lloyd KO, Lewis Jr JL. Binding parameters of monoclonal antibodies reacting with ovarian carcinoma ascites cells. *Cancer Immunol Immunother* 1989;28:199-207.
56. Roe R, Robins RA, Laxton RR, Baldwin RW. Kinetics of divalent monoclonal antibody binding to tumour cell surface antigens using flow cytometry: standardization and mathematical analysis. *Molecular Immunol* 1985;22:11-21.
57. Giacomini P, Natali P, Ferrone S. Analysis of the interaction between a human high molecular weight melanoma-associated antigen and the monoclonal antibodies to three distinct antigenic determinants. *J Immunol* 1985;135:696-702.
58. Vecchio SD, Reynolds JC, Balsberg RG, et al. Measurement of local M₁ 97,000 and 250,000 protein antigen concentration in sections of human melanoma tumor using in vitro quantitative autoradiography. *Cancer Res* 1988;48:5475-5481.
59. Press OW, Eary JF, Badger CC, et al. High-dose radioimmunotherapy of B cell lymphomas. *Front Radiat Ther Oncol* 1990;24:204-212.
60. Fogler WE, Klinger MR, Abraham KG, Gottlinger HG, Riethmuller G, Daddona PE. Enhanced cytotoxicity against colon carcinoma by combinations of noncompeting monoclonal antibodies to the 17-1A antigen. *Cancer Res* 1988;48:6303-6308.
61. Mason DW, Williams AF. The kinetics of antibody binding to membrane antigens in solution and at the cell surface. *Biochem J* 1980;187:1-20.
62. Masuho Y, Zalutsky M, Knapp RC, Bast Jr RC. Interaction of monoclonal antibodies with cell surface antigens of human ovarian carcinomas. *Cancer Res* 1984;44:2813-2819.
63. Wormsley SB, Collins ML, Royston I. Comparative density of the human T-cell antigen T65 on normal peripheral blood T cells and chronic lymphocytic leukemia cells. *Blood* 1981;57:657-662.
64. Johnstone EW, Andrew SM, Hogarth MP, Pietersz GA, McKenzie IFC. The effect of temperature on the binding kinetics and equilibrium constants of monoclonal antibodies to cell surface antigens. *Molecular Immunol* 1990;27:327-333.
65. Scheinberg DA, Tanimoto M, McKenzie S, Strife A, Old LJ, Clarkson BD. Monoclonal antibody M195: a diagnostic marker for acute myelogenous leukemia. *Leukemia* 1989;3:440-445.
66. Rosen ST, Zimmer AM, Goldman-Leikin R, et al. Radioimmunodetection and radioimmunotherapy of cutaneous T cell lymphomas using an I-131-labeled monoclonal antibody: an Illinois cancer council study. *J Clin Oncol* 1987;5:562-573.
67. Larson SM, Carrasquillo JA, McGuffin RW, et al. Use of I-131 labeled, murine Fab against a high molecular weight antigen of human melanoma: preliminary experience. *Radiology* 1985;155:487-492.
68. Clauss MA, Jain RK. Interstitial transport of rabbit and sheep antibodies in normal and neoplastic tissues. *Cancer Res* 1990;50:3487-3492.
69. Zanzonico PB, Bigler RE, Primus FJ, et al. Compartmental modeling approach to the radiation dosimetry of radiolabeled antibody. In: Schlafke-Stelson AT, Watson EE, eds. *Proceedings of the fourth international dosimetry symposium*. Oak Ridge, TN: CONF-851113-(DE86010102); 1985:421-425.
70. Loevinger R, Berman M. A revised schema for calculating the absorbed dose from biologically distributed radionuclides. *MIRD pamphlet no. 1, revised*. New York, NY: Society of Nuclear Medicine; 1976.
71. Snyder WS, Ford MR, Warner GG. Estimates of specific absorbed fractions for photon sources uniformly distributed in various organs of a heterogeneous phantom. *MIRD pamphlet no. 5, revised*. New York, NY: Society of Nuclear Medicine; 1976.
72. Snyder WS, Ford MR, Warner GG, Watson SB. "S," absorbed dose per unit cumulated activity for selected radionuclides and organs. *MIRD pamphlet no. 11, revised*. New York, NY: Society of Nuclear Medicine; 1975.
73. Foster DM, Boston RC, Jacquez JA, Zech LA. *The SAAM tutorials: an introduction to using conversational SAAM version 30*. Seattle: Resource Facility for Kinetic Analysis; 1989.
74. Bigler RE, Zanzonico PB, Leonard R, et al. Bone marrow dosimetry for monoclonal antibody therapy. In: Schlafke-Stelson AT, Watson EE, eds. *Proceedings of the fourth international dosimetry symposium*. Oak Ridge, TN: CONF-851113-(DE86010102); 1985:535-544.
75. Siegel JA, Wessels BW, Watson EE, et al. Bone marrow dosimetry and toxicity for radioimmunotherapy. *Antibody Immunoconj Radiopharm* 1990;3:213-233.
76. Simpkin DJ, Mackie TR. EGS4 monte carlo determination of the beta dose kernel in water. *Med Phys* 1990;17:179-186.
77. Berger MJ, Selzter S. ETRAN, Monte Carlo code system for electron and photon transport through extended media. Oak Ridge National Labs, Documentation for RSIC Computer Code Package CCC-107; 1973.
78. Berger MJ. *Improved point kernels for electron and beta-ray dosimetry*. NBSIR 73-107, Washington, DC: Center for Radiation Research, U.S. Department of Commerce; 1973.
79. Bensinger WI. Plasma exchange and immunoadsorption for removal of antibodies prior to ABO incompatible bone marrow transplant. *Transplant Procedures* 1981;19:4632-4637.
80. Nilsson R, Lindgren L, Lilliehorn P. Extracorporeal immunoadsorption therapy on rats. In vivo depletion of specific antibodies. *Clin Exp Immunol* 1990;82:440-444.
81. Wheldon TE, O'Donoghue JA. The radiobiology of targeted radiotherapy. *Int J Radiat Biol* 1990;58:1-21.
82. Wheldon TE, O'Donoghue JA, Barrett A, Michalowski AS. The curability of tumors of differing size by targeted radiotherapy using ¹³¹I or ⁹⁰Y. *Radiother Oncol* 1991;21:91-99.
83. Koizumi K, DeNardo GL, DeNardo SJ, et al. Multicompartmental analysis of the kinetics of radioiodinated monoclonal antibody in patients with cancer. *J Nucl Med* 1986;27:1243-1254.
84. Sgouros G, Bigler RE, Zanzonico PB. Compartmental model simulations of antibody kinetics: what parameters most influence antibody dosimetry? *J Nucl Med* 1987;28:617.
85. Bigler RE, Zanzonico PB, Cosma M, Sgouros G. Adjuvant radioimmunotherapy for micrometastases: a strategy for cancer cure. In: Srivastava SC, ed. *Radiolabeled antibodies for imaging and therapy*. Barga, Italy: NATO Advanced Study Institute; New York: Plenum Press; 1988:409-429.
86. Rescigno A, Bushe H, Brill AB, Rusckowski M, Griffin TW, Hantowich DJ. Pharmacokinetic modeling of radiolabeled antibody distribution in man. *Am J Physiol Imaging* 1990;5:141-150.
87. Blasberg RC, Nakagawa H, Bourdon MA, Groothuis DR, Patlak CS, Bigner DD. Regional localization of a glioma-associated antigen defined by monoclonal antibody 81C6 in vivo: kinetics and implications for diagnosis and therapy. *Cancer Res* 1987;47:4432-4443.
88. Sgouros G, Bigler RE, Zanzonico PB, Strauss A. Kinetics of radiolabeled antibody penetration into micrometastatic cell clusters: a model incorporating diffusion, saturable binding, and dissociation. *J Nucl Med* 1989;30:777.
89. Kwok CS, Cole SE, Liao S. Uptake kinetics of monoclonal antibodies by human malignant melanoma multicell spheroids. *Cancer Res* 1988;48:1856-1863.
90. McFadden R, Kwok CS. Mathematical model of simultaneous diffusion and binding of antitumor antibodies in multicellular human tumor spheroids. *Cancer Res* 1988;48:4032-4037.
91. Langmuir VK, McGann JK, Buchegger F, Sutherland RM. ¹³¹I-anticarcinoma embryonic antigen therapy of LS174T human colon adenocarcinoma spheroids. *Cancer Res* 1989;49:3401-3406.
92. Woldberg WH. Metastasis. In: Kahn SB, Love RR, Sherman C, Chakravorty R, ed. *Concepts in cancer*. New York: Grune and Stratton; 1984:149-153.
93. Folkman J. How is blood vessel growth regulated in normal and neoplastic tissue? *Cancer Res* 1986;46:467-473.
94. Woo DV, Li D, Brady LW, Emrich J, Mattis J, Steplewski Z. Auger electron damage induced by radioiodinated Iodine-125 monoclonal antibodies. *Front Radiat Ther Oncol* 1990;24:47-63.
95. Brady LW, Woo DV, Heindel ND, Markoe AM, Koprowski H. Therapeutic diagnostic uses of modified monoclonal antibodies. *Int J Radiat Oncol Biol Phys* 1987;13:1535-1544.